Apple-shaped obesity; a risky soil for cytokine-accelerated severity in COVID-19

Tadashi Hosoya
Tokyo Medical and Dental University
Seiya Oba
Tokyo Medical and Dental University
Yoji Komiya
Tokyo Medical and Dental University
Daisuke Kawata
Tokyo Medical and Dental University
Mari Kamiya
Tokyo Medical and Dental University
Hideyuki Iwai
Tokyo Medical and Dental University
Sho Miyamoto
National Institute of Infectious Disease
Michiyo Kataoka
National Institute of Infectious Disease
Minoru Tobiume
National Institute of Infectious Disease
Takayuki Kanno
National Institute of Infectious Disease
Akira Ainai
National Institute of Infectious Disease
Hiroyuki Sato
National Institute of Infectious Disease
Akihiro Hirakawa
Tokyo Medical and Dental University
Takashi Satoh
Tokyo Medical and Dental University
Kenji Wakabayashi
Tokyo Medical and Dental University
Tetsuya Yamada
Tokyo Medical & Dental University
Yasuhiro Otomo

Tokyo Medical and Dental University
Yasunari Miyazaki
Tokyo Medical and Dental University
Hideki Hasegawa
Influenza Virus Research Center, National Institute of Infectious Diseases
Tadaki Suzuki
National Institute of Infectious Disease
Shinsuke Yasuda (syasuda.rheu@tmd.ac.jp)
Tokyo Medical and Dental University

Letter

Keywords:

Posted Date: November 9th, 2022

DOI: https://doi.org/10.21203/rs.3.rs-2252161/v1

Additional Declarations: Yes there is potential Competing Interest. S.Y. received research funding from Abbvie, Asahi Kasei, Pharma, Chugai Pharmaceutical, CSL Behring, Eisai, ImmunoForge, Mitsubishi Tanabe, Pharma, and Ono pharmaceutical, speaking fees from Abbvie, Asahi Kasei Pharma, Chugai Pharmaceutical, Eisai, Eli Lilly, GlaxoSmithKline, Mitsubishi Tanabe Pharma, Ono pharmaceutical, and Pfizer. YM received a research grant and an honorarium from Chugai Pharmaceutical Co., Ltd. The other authors have declared no conflicts of interest.

Apple-shaped obesity; a risky soil for cytokine-accelerated severity in COVID-19

Tadashi Hosoya[1*], Seiya Oba[1*], Yoji Komiya[1], Daisuke Kawata[1], Mari Kamiya[1], Hideyuki Iwai[1], Sho Miyamoto[2], Michiyo Kataoka[2], Minoru Tobiume[2], Takayuki Kanno[2], Akira Ainai[2], Hiroyuki Sato[3], Akihiro Hirakawa[3], Takashi Satoh[4], Kenji Wakabayashi[5], Tetsuya Yamada[6], Yasuhiro Otomo[7], Yasunari Miyazaki[8], Hideki Hasegawa[9**], Tadaki Suzuki[2**], Shinsuke Yasuda[1‡**]

Asterisks (* and **) indicated equal contribution

‡Corresponding author

1 Department of Rheumatology, Graduate School of Medical and Dental Sciences, Tokyo Medical and Dental University (TMDU), Tokyo, Japan,

2 Department of Pathology, National Institute of Infectious Diseases, Tokyo 208-0011, Japan

3 Department of Clinical Biostatistics, Graduate School of Medical and Dental Sciences, Tokyo Medical and Dental University (TMDU), Tokyo, Japan

4 Department of Immune Regulation, Graduate School of Medical and Dental Sciences, Tokyo Medical and Dental University (TMDU), Tokyo, Japan.

5 Department of Intensive Care Medicine, Graduate School of Medical and Dental Sciences, Tokyo Medical and Dental University (TMDU), Tokyo, Japan

6 Department of Molecular Endocrinology and Metabolism, Graduate School of Medical and Dental Sciences, Tokyo Medical and Dental University (TMDU), Tokyo.

7 Trauma and Acute Critical Care Medical Center, Graduate School of Medical and Dental Sciences, Tokyo Medical and Dental University (TMDU), Tokyo, Japan

8 Department of Respiratory Medicine, Graduate School of Medical and Dental Sciences, Tokyo Medical and Dental University (TMDU), Tokyo, Japan

9 Influenza Virus Research Center, National Institute of Infectious Diseases, Tokyo, Japan

Introductory paragraph

Obesity is one of the most significant risk factors for the deterioration and mortality associated with COVID-19 [1]. A certain proportion of COVID-19 patients experience marked elevations of inflammatory mediators, termed “cytokine storm”, resulting in the deterioration of the respiratory condition [2,3]. In the present study, we elucidate that the high visceral adipose tissue (VAT) burden was more closely related to accelerated inflammatory responses and the mortality of Japanese COVID-19 patients than other obesity-associated markers, including body mass index (BMI). To explore a novel stratification of COVID-19 patients, we infected mouse-adapted SARS-CoV-2 in several obese mice, revealing that VAT-dominant ob/ob mice and diet-induced obesity obese mice died after infection with low-titer mouse-adapted SARS-CoV-2 virus due to the subsequent cytokine storm, whereas none of the subcutaneous adipose tissue (SAT) dominant db/db mice or control lean wild-type mice died. SARS-CoV-2 genome and proteins were more abundant in the lungs of ob/ob mice, engulfed in macrophages, resulting in increased production of inflammatory cytokine represented by IL-6. As well as the anti-IL-6 treatment, the prevention of obesity by leptin administration improved the survival of SARS-CoV-2 infected ob/ob mice by reducing the viral protein burden and excessive immune responses.

Results

Visceral, but not subcutaneous adipose tissue accumulation was associated with death in Japanese COVID-19 patients.

We have previously reported the clinical characteristics of Japanese COVID-19 patients focusing on the thrombotic complications [4]. During inpatient management and data collection, we also noticed that the patients with abdominal fat dominant obesity, namely, apple-shaped (VAT dominant) obesity, tend to experience severer disease courses and worse outcomes rather than those with pear-shaped (SAT dominant) obesity. The former is closely associated with metabolic disorders and immune-related diseases [5,6], whereas the latter type of obesity does not preclude such association with specific diseases. Therefore, we hypothesized that the accumulation of VAT would fuel the systemic inflammatory responses in COVID-19, and the burden of VAT would become a more reliable marker to identify the patients with a potential risk.

To evaluate whether body composition was associated with the outcome of COVID-19, we quantified the fat areas in the abdomen and in the subcutaneous tissues using abdominal CT scan images and (Fig. 1A) [7]. These data were analyzed in correlation with disease severity and outcome. VAT area, SAT area, and BMI were associated with the peak severity of COVID-19 (Fig. 1B-D). Among the obesity-related markers, the VAT area was the single marker with a statistically significant association with death (Extended Data Table 1). By drawing the Receiver Operating Characteristic (ROC) curve, we designated the cut-off value of VAT area as 175 cm^2 in order to maximize sensitivity and specificity (81.0% and 55.9%, respectively). Indeed, multivariable analysis using a logistic regression model revealed that increased VAT area (*p<0.0001*) was a robust independent risk factor for mortality due to COVID-19 in addition to other known risk factors [8–12] such as older age (*p=0.0389*), chronic kidney disease (CKD) above grade 4 (*p=0.0382*), and history of infarction (*p=0.0097*), with high adjusted odds ratio (Extended Data Table 2). Kaplan-Meier survival analysis also revealed the survival rate during hospitalization was worse in the patients with high VAT burden but not in those with high BMI or high SAT burden (Fig. 1E-G). The Harrell's c-statistic with optimism correction using the internal bootstrap method of the Cox regression model [13] including the known risk factors (gender male, hypertension, history of infarction, elevated HbA1c (> 7.5%), and CKD (≥ grade 4)) was 0.6632 (Extended Data Table 3). By adding increased VAT (> 175 cm^2) to this model, we could improve the value to 0.7229, whereas the addition of BMI (> 30 kg/m^2) or SAT (>160 kg/m^2) decreased (0.6470 and 0.6157, respectively).

Interestingly, increased adipose tissue has weak, but significant, correlations with several biomarkers, including CRP, D-dimer and, ferritin at both the early phase and the disease peak in the relatively younger group (Fig. 1H, 1I, and Extended Data Fig. 1A-C). Since macrophages and adipocytes in VAT contributed to subclinical inflammation in some metabolic diseases [14], we hypothesized that increased VAT burden also fueled the inflammatory responses during COVID-19 and resulted in worsening outcomes in some patients.

Visceral obese mice were more susceptible to SARS-CoV-2 infection

The ob/ob and db/db mice have a genetic dysfunction of leptin ligand or receptor, respectively, leading to hyperphagia and a similar level of obesity (Extended Data Fig. 2A). Visceral adipose accumulation including fatty liver was dominant in ob/ob mice rather than in db/db mice (Extended Data Fig. 2B and 2C), as shown previously [15,16]. The number of crown-like structures (CLS), which are formed with inflammatory macrophages as a result of excessive apoptotic adipocyte exposure, were more frequently observed in the livers from ob/ob mice than those from db/db mice, indicating the existence of subclinical inflammation [15].

Immune responses against mouse-adapted SARS-CoV-2, established from human isolates, reached peak levels at three days post-infection (dpi), as shown previously [17]. Intriguingly, all the ob/ob mice died around four to nine dpi, after inoculation with mouse-adapted SARS-CoV-2 (Fig. 2A and 2B). In contrast, all the db/db mice, as well as the control C57BL/6 mice, survived. Histological analysis at the disease peak (three dpi) revealed the minor differences among the three strains, and the lung inflammation was distributed widely in B6 and ob/ob mice rather than db/db mice (Extended Data Fig. 3A and 3B), indicating that the infection itself was less likely a cause of death in ob/ob mice. However, the SARS-CoV-2-positive cells in the alveolar area were more abundant in ob/ob mice than in the other two strains (Fig. 2C-2E), while those in the bronchial area were similar among three groups. Indeed, more copies of SARS-CoV-2 genomic RNA-encoding spike (S) protein were detected in the lungs of ob/ob mice at three dpi (Fig. 2F). To consider the susceptibility of lung cells to SARS-CoV-2 infection, we analyzed the distribution of SARS-CoV-2 antigens at one dpi. Both bronchial and alveolar cells of ob/ob mice showed greater levels of SARS-CoV-2 IHC staining (Extended Data Fig. 4A-4C). However, both the viral infectivity assay using lung homogenates at one dpi or at three dpi

and experimental SARS-CoV-2 infection using isolated lung epithelial cells demonstrated indifferent results among three groups (Extended Data Fig. 4D and 4E). These findings indicated that the susceptibility of lung cells to SARS-CoV-2 infection and replication capability was indifferent among three strains.

Thus, we considered that the detection of viral-derived genomes or proteins would result from phagocytosis to explain the discrepancy. Interestingly, SARS-CoV-2 genomic RNA was also detected in the liver and in circulating cells, particularly in ob/ob mice (Fig. 2G and 2H). The proportion of SARS-CoV-2 antigen-positive macrophages was increased in ob/ob mice, although F4/80-positive macrophages as well as EpCAM-positive lung epithelial cells co-localized with SARS-CoV-2 antigens in all three strains (Fig. 2I-2K). Additionally, SARS-CoV-2 viral particles were observed using an electron microscope to be present only in the macrophages and disrupted epithelial cells (Fig. 2L). However, no virus-derived ultrastructures, such as double-membrane vesicles and budding virions, during viral replication were found in the macrophage. The high density and irregular nucleocapsid arrangement of the viral particles in macrophage endosomes further indicated that they were distinct from infectious post-budding viral particles. These observations suggested that the macrophages in ob/ob mice carried disrupted viral particles during phagocytosis and did not support viral replication.

Therefore, we considered that SARS-CoV-2 antigen-carrying phagocytes circulated systemically in ob/ob mice and might induce inflammasome-dependent activation, as shown previously [18,19].

Innate immune activation and cytokine storm occurred in the lungs of ob/ob mice.

On three dpi we evaluated the inflammatory cytokine levels, revealing that IL-6 and type I/II interferon responses were upregulated in the lungs of ob/ob mice but not in db/db and wild-type mice at RNA levels and protein levels (Fig. 3A-3C). Additionally, we observed an impairment of type I interferon responses in db/db mice (Fig. 3A and 3B), consistent a previous report [20]. In the RNA-Seq analysis, the major principal components exhibited separated gene expression patterns between the three strains (Fig. 3D). Among 184 genes identified as shared differentially expressed genes (DEGs), we identified using pathway or gene set enrichment analysis that global alterations of inflammation-associated pathways were enriched in the shared DEGs and were enhanced in ob/ob mice but not in the other

mice (Fig. 3F and 3G). The representative DEGs in the top four pathways of Fig. 3F are shown as a heatmap in Fig. 3H.

We next explored the differences between ob/ob and db/db mice by further RNA-Seq regardless of SARS-CoV-2 infection. The pathway enrichment analysis of the 738 DEGs identified different gene expressions in several immune-response associated pathways, including the phagosome pathway (Extended Data Fig. 5A-5C). Based on the differences in genetic backgrounds of ob/ob and db/db mice (e.g., C57BL/6 and C57BLKS, respectively), different expressions of major histocompatibility complex class II molecules were identified (Extended Data Fig. 5D). Beyond the differences, we observed a clear separation of macrophage phenotypes associated molecules, specifically, inflammatory macrophage associated molecules were dominant in ob/ob mice, while pan-macrophage markers were upregulated in both ob/ob and db/db mice after infection (Extended Data Fig. 5E).

These findings suggested that ob/ob mice were more sensitive against SARS-CoV-2 infection rather than db/db mice, and excessive inflammatory responses were the cause of death in ob/ob mice. Indeed, survival rates were improved by inhibition of IL-6 using the anti-IL-6-receptor antibody MR16-1, the mouse counterpart to tocilizumab (Fig. 3I) [21], indicating that excessive IL-6 production was at least one of the causes of death in ob/ob mice.

Reducing the adipose tissue by leptin administration prevented death of ob/ob mice with prompt elimination of virus genome and attenuation of excessive immune responses.

Reduction of the body weight by preventive administration of leptin to ob/ob mice (lean ob/ob) resulted in improved survival after infection, suggesting that excessive adipose accumulation was the cause of death in ob/ob mice (Fig. 4A, and Extended Data Fig. 6A and 6B). Indeed, leptin administration after infection did not show any beneficial effects on the survival of ob/ob mice, suggesting the difference in survival was not due to an immune-related feature of leptin. In fact, leptin pretreatment could reduce the adipose tissue weight and improve the fatty liver with decreased CLS (Extended Data Fig. 6C-6E). As expected, regarding SARS-CoV-2, the IHC score, genomes, and the ratio of SARS-CoV-2 positive macrophages were lower in the lean ob/ob mice than in the obese ob/ob mice (Fig. 4B-4E). Simultaneously, IL-6 induction and interferon-induced responses were attenuated in lean

ob/ob mice (Fig. 4E and 4F).

Furthermore, we identified that several inflammation-associated pathways were enriched among 689 shared DEGs between lean ob/ob mice and obese ob/ob mice, similar to Fig. 3F (Fig. 4G-4I). Interestingly, gene set enrichment analysis revealed that most of them were attenuated in lean ob/ob mice rather than obese ob/ob mice (Fig. 4J).

In contrast, we elucidated that abdominal fat gain in wild-type mice by high-fat diet resulted in the early death after the mouse-adapted SARS-CoV-2 infection, confirming the negative effects of VAT in mice with common genetic background (Extended Data Fig. 7A-7D).

From these findings, we concluded that the excessive adipose accumulation was responsible for delayed elimination of the virus and to the activation of inflammatory macrophage and cytokine storm, leading to death in SARS-CoV-2 infected obese mice.

Discussion

Here, we have shown that VAT burden is a risk factor contributing to the deterioration and death of Japanese COVID-19 patients, and that excessive adipose tissue is a more accurate predictor of mortality, which has been previously suggested in several studies [22,23]. Interestingly, the contribution of overweight to COVID-19 mortality was more pronounced in Asian and Black populations than in White, even with a similar level of obesity [24,25]. Since VAT-dominant obesity is more common in Asian and associated with metabolic disorders [5,26], VAT accumulation might accurately reflect the discrepancy of epidemiological or ethnic risks of COVID-19 mortality in overweight patients, at least in the Japanese population. We should consider increased VAT as a risk factor for the deterioration and mortality seen in obese patients, especially among younger people [24,25], since most of the other risk factors, such as hypertension, renal dysfunction, and a history of cardiovascular diseases, are associated with aging [27].

Recently, various reports demonstrated that macrophage activation is the essential factor of the cytokine storm complicated in the severe COVID-19 patients and animal models of SARS-CoV-2 infection [18,28–30]. In addition, several studies revealed that adipose tissues serve as a target and reservoir for SARS-CoV-2, with evidence of infection in adipocytes [31,32] and infiltrating monocytes [29]. Interestingly, Salina et al. revealed that the engulfment of SARS-CoV-2 infected pro-apoptotic cells by macrophages resulted in the production of inflammatory cytokines and impaired efferocytosis, namely, the failure in phenotype conversion to anti-inflammatory macrophages [33]. Impaired efferocytosis was considered as a major mechanism of metabolic disorders induced by obesity [34] and was observed in ob/ob mice [35]. In this study, we showed that SARS-CoV-2 transcripts were abundant systemically, and expressions of M2 macrophage markers were impaired in ob/ob mice. Therefore, we considered that macrophages were activated by engulfing the SARS-CoV-2 infected cells and unleashed inflammatory responses, resulting in the production of lethal cytokines in VAT-dominant mice.

Comparing different types of obese mice, we demonstrated quite a clear discrepancy in the inflammatory response to mouse-adapted SARS-CoV-2 infection between ob/ob mice and db/db mice, even with the comparable obese states in body weight. While the vulnerability of pancreatic beta cells from C57BLKS background resulted in the impaired glucose metabolism [36], little is known about the difference in immunological phenotype between ob/ob mice and db/db mice. Although both strains of mice are considered similarly immunocompromised [37–39], previous report demonstrated that ob/ob mice showed a

greater sensitivity to inflammatory stimuli by endotoxin than their lean littermates, or db/db mice [40]. In spite of the immunological function of leptin, the vulnerability of ob/ob mice against SARS-CoV-2 was not merely due to such effects because the simultaneous administration of leptin to the obese ob/ob mice did not improve their disease course.

In addition to anti-viral agents, anti-inflammatory therapies, including steroids, IL-6 blockers, and baricitinib, are being administered to patients with moderate to severe COVID-19. Such anti-cytokine strategies attenuate excessive immune responses and provide benefits to certain subgroups of patients. However, at this moment, we cannot predict the efficacy of the anti-inflammatory/immunosuppressive treatments in the real-world clinics. Since patients prone to cytokine storms are more likely to respond to these therapies, our current data are expected to be helpful in the stratification of the patients who would benefit from anti-cytokine therapeutics in the earlier phase of COVID-19.

Also, we might warn of the necessity of improving our lifestyle in this era of emerging novel or mutated viral variants since VAT accumulation is related to the custom of cardiorespiratory fitness regardless of the BMI level [41,42]. To attenuate inflammatory responsiveness upon known and unknown infection, interventions aimed at reducing VAT may be a feasible goal for the obese population.

We must admit several limitations in this study. Because clinical questions were raised from our retrospective cohort of COVID-19 patients, we could not avoid the residual confounding and lack of data regarding some biomarkers or follow-up data. We should further identify the mechanisms how visceral adipose accumulation recruited or converted macrophages into inflammatory phenotype in the lungs and visceral adipose tissue.

In conclusion, our findings indicated that VAT-dominant patients would be at risk for cytokine storm due to COVID-19 and might be good candidates to receive cytokine-suppressing therapy during the disease course.

MATERIALS AND METHODS

The patient cohort of COVID-19 in Tokyo Medical and Dental University hospital

In the present study, we analyzed 250 patients who underwent abdominal computed tomography (CT) out of 594 consecutive COVID-19 patients admitted to Tokyo Medical and Dental University (TMDU) Hospital from Apr. 2020 to Aug 2021. Among them, 34 patients died in hospital, while 216 survived.

The diagnostic real-time reverse-transcription PCR (RT-PCR) was conducted during admission, as described previously [4]. We collected all the data from electronic medical records, including disease severity, comorbidities, laboratory data, treatment, and outcomes. We assessed disease severity at admission and at times of the most severe clinical condition. The definition of disease severity was followed by the guideline presented by the Japanese Ministry of Health, Labor, and Welfare. Briefly, mild for patients who do not need oxygen therapy; moderate for patients who need oxygen of equal or <5 L/min; and severe for patients who need oxygen of more than 5 L/min or mechanical ventilation. The definitions of comorbidities, treatment, and complications were described previously [4].

Study protocols and procedures complied with the Declaration of Helsinki and followed the Strengthening the Reporting of Observational Studies in Epidemiology (STROBE) reporting guideline. This study was approved by the ethics committees of TMDU as M2020-027.

Quantification of fat tissues from CT images

The abdominal fat distribution was measured on the umbilicus level of abdominal CT images using Fat Scan version 2.0 software (N2 System Co., Osaka, Japan) [7]. Briefly, the regions of interest (ROI) of the fat areas were defined by tracing their contour and the outline of the abdominal wall. The visceral and subcutaneous fat areas were calculated automatically from ROI following the caliper of each CT image.

Animals

Male C57BL/6JHamSlc-ob/ob (ob/ob), C57BLKS/J-db/db (db/db), and C57BL/6J (B6) mice were purchased from Japan SLC, Inc. (Hamamatsu, Japan) or CLEA Japan, inc. (Tokyo, Japan) and were maintained in specific pathogen-free facilities in National institute of infectious diseases. All animals were allowed free access to water and diet and provided with

12 hours of light/dark cycle.

Cells and viruses

VeroE6/TMPRSS2 cells were purchased from the Japanese Collection of Research Bioresources Cell Bank (the National Institute of Biomedical Innovation, Health, and Nutrition, Osaka, Japan) were used in this study. Cells were cultured in DMEM, low glucose (Sigma-Aldrich, St. Louis, MO), containing 10% fetal bovine serum (FBS), penicillin G (50 IU/ml), and streptomycin (50μg/ml) (10DMEM). SARS-CoV-2 human isolates were prepared and provided by Dr. Shutoku Matsuyama and Dr. Makoto Takeda (Department of Virology III, National Institute of Infectious Diseases, Japan) [17]. In addition, stocks of QHmusX PT2-Lot2 (GenBank Accession No.: LC605054) were propagated and titrated on VeroE6/TMPRSS2 cells in DMEM containing 2% FBS, penicillin G (50 IU/ml), and streptomycin (50 μg/ml) (2DMEM). Viral infectivity titers were expressed as TCID50 per milliliter in VeroE6/TMPRSS2 cells and were calculated according to the Behrens-Kärber method. Work with infectious SARS-CoV-2 was performed under BSL3 conditions.

SARS-CoV-2 challenge experiments

Mouse-adapted SARS-CoV-2 strain was established in the previous study [17]. Mice were anesthetized by intraperitoneal injection with a mixture of 0.75 mg/kg of medetomidine, 4.0 mg/kg of midazolam, and 5.0 mg/kg of butorphanol and then inoculated viral solution intranasally (i.n.). Viral solutions for inoculation were diluted with PBS and 30 μl of solution contained twice of the 50% lethal dose ($2LD_{50}$) determined in 24-week-old BALB/c mice. Body weight was measured, and behaviors were observed daily for ten days. The humane endpoint was defined as the appearance of clinically diagnostic signs of respiratory stress or more than 25% weight loss. Mice were sacrificed with an overdose of isoflurane if severe disease symptoms or weight loss were observed. The ob/ob, db/db, and B6 mice were sacrificed at one, three, or ten days post infection (dpi) to collect whole blood/serum and tissue homogenates. (n = 3-6 per group).

In vivo anti-IL-6R antibody (MR-16-1) treatment

A Rat anti-mouse IL-6 receptor monoclonal Ab (clone MR16-1, rat IgG1) was provided by Chugai Pharmaceutical (Tokyo, Japan). Purified rat IgG1 (isotype-matched control Ab) (Sigma-Aldrich) was administered as an isotype-matched-control. The 2 mg of antibodies and vehicle were administered intraperitoneally one hour before the virus inoculation and on three dpi. The body change and abnormal behaviors were monitored daily up to 10 dpi to

consider humane endpoints.

The administration of leptin

For the continuous administration of leptin, we used Alzet pumps (DURECT Corp., Cupertino, CA) with model 2004 for six weeks treatment and model 2001 for one week treatment. These pumps delivered 2 μg of mouse recombinant leptin (biotech) per day and were inoculated in the back of 9-week-old ob/ob mice for the six-week administration and 15-week-old ob/ob mice for the administration just before the SARS-CoV-2 infection, respectively. Body weights were measured every week after pump inoculation until the SARS-CoV-2 infection.

Diet induced obesity model

To develop visceral dominant obesity, eight-to-ten-week male C57BL/6J (B6) mice were by high fat diet (HFD) (D12492, Research Diet), which contained 60% of fat, ad libitum access to food and water for ten weeks. Body weights were measured every week during HFD feeding until the SARS-CoV-2 infection.

Tissue residual viral infectivity assay

Left lung lobes from ob/ob, db/db, and B6 mice were collected and homogenized in 2 ml PBS with a gentleMACS TM Octo Dissociator (130-095-937, Miltenyi Biotec). Homogenates were centrifuged at 3000 rpm for 10min, and the supernatants were collected and frozen at -80℃. When we conducted the analysis, the supernatants (10% w/v) were diluted in Dulbecco's Modified Eagle medium (DMEM) containing 2% FBS, 50 IU/ml penicillin G, and 50 μg/ml streptomycin (2DMEM). The serially diluted samples were added to Vero E6-TMPRSS2 cells in triplicate, and cells were incubated for five days to observe cytopathic effects (CPEs). To visualize the plaques, we fixed the cells with 20% formaldehyde and stained them with 1% crystal violet. Viral infectivity titers were expressed as TCID50 per milliliter in VeroE6/TMPRSS2 cells and were calculated according to the Behrens-Kärber method.

Histopathology and immunohistochemistry

Mice were anesthetized as described above and were perfused transcardially with phosphate-buffered saline (PBS). Lungs, livers, spleens, and adipose tissues were collected and fixed with 4% paraformaldehyde for 72 hours. Subsequently, fixed tissues were

363 embedded into paraffin following standard protocols and sectioned at 3 μm thickness. After
364 deparaffinization and rehydration, the sections were stained with hematoxylin and eosin
365 (H&E) or immunofluorescent staining.

366 For the immunohistochemical staining, endogenous peroxidases were inactivated with
367 3% hydrogen peroxide for 20 min. After the incubation in a blocking solution (1% BSA in TBS-
368 T) for 60 min at room temperature, the tissue sections were incubated with primary antibodies
369 against rabbit anti- SARS-CoV/SARS-CoV-2 Nucleocapsid Antibody (Sinobiological, #Cat:
370 40143-R001,1:5000), rabbit anti-EpCAM antibody (Abcam, #cat. Ab 71916,1:500), and rabbit
371 anti-F4/80 antibody (Abcam, #cat. ab6640, 1:100) overnight at 4℃. Tissue sections
372 incubated with rabbit IgG were used as isotype controls. After three washes, the sections
373 were incubated with secondary antibodies at 37℃ for 30 min, counterstained with DAPI, and
374 then sealed with Fluoro-Gel for photography. Microscopy images were photographed at ×4
375 and ×40 magnification using BX-50(OLYMPUS). Fluorescent images were obtained using a
376 BZ-X810 (Keyence).

377 To measure the abundance of SARS-CoV-2 antigen and the infiltration of F4/80 positive
378 cells semi-quantitatively, we evaluated ten images blindly captured from individual samples
379 with 100× objective fields. The scores of individual mice were expressed as the average of
380 the ten images. IHC scores were determined based on the percentage of positive cells, using
381 the following scoring system: 0, no positive cells; 1, positive cells (≤5%); 2, positive cells
382 (>5%, ≤20%); 3, positive cells (>20%, ≤50%); 4, positive cells (>50%). The proportions of
383 positive cells were determined using PatholoCount version 1.2.0 software (MITANI
384 Corporation, Toshima-ku, Tokyo).

385 **Pathological score**

386 Lung tissue sections were scored based on pathological changes. To evaluate
387 histological changes, we used two different quantitative histologic scores on lung tissues as
388 reported previously [43,44]. Briefly, the distribution score was based on the percentage of
389 inflammation area for each section of the five lobes with the following scoring system: 0, no
390 pathological change; 1, affected area (≤10%); 2, affected area (<50%, >10%); 3, affected
391 area (≥50%); an additional point was added when pulmonary edema and alveolar
392 hemorrhage was observed. The total score for the five lobes was shown as a distribution
393 score for individual animals. A Lung Injury Scoring System by the American Thoracic Society
394 was used to quantitate histological features of acute lung injury (ALI) observed in mouse
395 models. We randomly chose three fields of lung tissue at high power (200×), which were

scored as previously described : (A) neutrophils in the alveolar space (none = 0, 1–5 cells = 1, > 5 cells = 2), (B) neutrophils in the interstitial space/septae (none = 0, 1–5 cells = 1, > 5 cells = 2),(C) hyaline membranes (none = 0, one membrane = 1, > 1 membrane = 2), (D) Proteinaceous debris in air spaces (none = 0, one instance = 1, > 1 instance = 2), (E) alveolar septal thickening (< 2× mock thickness = 0, 2–4× mock thickness = 1, > 4× mock thickness = 2). Scores were calculated as followed: [(20x A) + (14 x B) + (7 x C) + (7 x D) + (2 x E)]/100. Final scores were obtained by averaging three fields per mouse. Microscopy slides were examined without knowledge of the identity of the animals.

Electron microscopy analysis of SARS-Cov-2 infection

Tissue samples were prefixed with 2.5% glutaraldehyde and 2% paraformaldehyde in 0.1M phosphate buffer for three days at 4°C and then post-fixed in 2% osmium tetroxide, dehydrated with a graded series of alcohols and propylene oxide, and embedded in epoxy resin. After trimming the epoxy resin-embedded tissue, ultrathin sections (70 nm thick) were cut using an ultramicrotome (Diatome), mounted on grids, and stained with 4% uranyl acetate and lead citrate for TEM analysis using a HT7700 (Hitachi Ltd., Japan) at 80 kV.

RNA extraction and RT-qPCR

Tissue samples were dissected from mice and immediately immersed in RNA later (Invitrogen) stabilization reagent and stored at -80℃ for 24 hr. Then, samples were transferred to a new tube containing 1-mm glass beads and 700μL Trizol (Invitrogen). Tissues were subsequently homogenized using a MINI BEAD-BEATER (Biospec). Total RNA was extracted and purified using a RNeasy mini kit (QIAGEN) and quantified using a spectrophotometer (NanoDrop one, Thermo Fisher Scientific). Real-time quantitative PCR (RT-qPCR) was performed using a Reverse transcription (RT)-PCR kit (QIAGEN) containing SYBR green dye. Each reaction was performed in duplicate. Relative gene expression was analyzed based on the threshold cycle method with GAPDH as an internal control. At least two independent experiments were analyzed.

RNA sequencing analysis.

Total RNA sequencing was performed with the assistance of BGI (Hong Kong, China). Briefly, total RNA was extracted from the lung as described above and checked for quality using RNA integrity scores were typically 7.0 and greater with an Agilent 2100 bioanalyzer (Agilent, Santa Clara, USA). For the quality control, mRNA had to meet the requirement of 28S/18S > 1, while miRNA had to meet the requirement of 28S/18S > 1.5. According to the

manufacturer's protocol, the RNA was fragmented into small pieces. Afterward, the fragmented RNA was reverse-transcribed into cDNA and amplified with polymerase chain reaction (PCR) to create a cDNA library. Quality control and quantification of the libraries were performed with the Agilent 2100 bioanalyzer and real-time quantitative PCR (qPCR) (TaqMan Probe). The qualified libraries were subjected to mRNA sequencing on a DNBSEQ platform (BGI-Shenzhen, China). The sample reads were trimmed to remove reads with an unknown base (N) content greater than 5%, adapters, and low-quality bases using Trimmomatic software and aligned with the reference genome using HISAT and Bowtie2 software. Mapping rates were > 90% in all samples. In total, 18126 genes (for Fig. 3), 18342 genes (for Fig.4) and 18283 genes (for Extended Data Fig. 5) were expressed (TPM > 0) in more than one sample and further analyzed.

Differentially expressed genes (DEGs)

Genes expressing significantly different amounts between the paired groups were determined using the PossionDis method based on poisson distribution (Audic and Claverie 1997), and DESeq2. FDR ≤ 0.001 in PossionDis and Qvalue (adjusted P value) ≤ 0.05 in DESeq2 were considered as cutoffs.

Enrichment analysis

The phyper function in R software was used to evaluate the enrichment of gene sets. Qvalue ≤ 0.05 is regarded as a significant enrichment. For the pathway classification, KEGG annotation was used. For gene set enrichment analysis, Gene ontology (GO) database related to biological process (GO_P) was used.

Multiplex assay for cytokine and chemokines

Homogenized lung samples from 19-week-old ob/ob, db/db, and B6 mice were diluted 1:1 in cell extraction buffer (10 mM Tris, pH 7.4, 100 mM NaCl, 1 mM EDTA, 1 mM EGTA, 1 mM NaF, 20 mM Na4P2O7, 2 mM Na3VO4, 1% Triton X-100, 10% glycerol, 0.1% SDS, and 0.5% deoxycholate (Invitrogen)), incubated for 10 min on ice with vortex, irradiated for 10 min with UV-C light to inactivate infectious virus, and tested in the BSL2 laboratory. Mouse Luminex Discovery Assay (R&D Systems) was utilized to analyze cytokines and chemokines in lung samples according to the manufacturer’s protocol, which detects 15 cytokines and chemokines: IP-10, IFN-γ, IL-6, IL-17/IL-17A, TNF-α, MCP-1, IL-1α/IL-1F1, IL-10, and IL-33. The assay samples were analyzed on a Luminex 200 instrument with xPONENT software described by the manufacturer.

Ex vivo cultures and infection of mice

The virus infection procedures were performed as previously described. Single-cell suspensions of lung tissues were obtained from non-infected 10-week-old male ob/ob, db/db, and B6 mice. Then, CD45 negative cells were isolated using MACS beads (Miltenyi Biotec) and harvested to 24 well plates at $5x10^5$cells/well. The adhered cells were infected with mouse-adapted SARS-CoV-2 at an MOI of 0.2, 0.5, 2, and 5 for 3 h at 37 °C. Each tissue fragment was washed in culture medium to remove residual virus inoculum, topped up with fresh medium, and incubated at 37 °C for 72hr. Total RNA was extracted using 700μL of QIAzol.

Ethics statements for animal experiments

All infected experiments were handled in BSL3 animal facilities, and non-infected experiments were in TMDU according to the guidelines of the committee. Experiments using pathogens were approved by the Committee for Pathogens at the National Institute of Infectious Diseases, Tokyo, Japan. Animal experiments were approved by the Animal Care and Use Committee of the National Institute of Infectious Diseases in Japan (120148 and 121093)), and the ethics committees of TMDU (G2020-023C5).

Statistics

We compared the distributions of continuous and categorical variables between the two groups using the Mann-Whitney U test and Chi-squared test (or Fisher's exact test), respectively. The cut-off values were determined by drawing the ROC curve about VAT, SAT and BMI to maximize sensitivity and specificity. Univariate and multivariate logistic regression analyses were employed to explore the impacts of known risk factors on mortality during admission. The variables were selected based on the previous reports and our research interests. Multicollinearity was then checked using the variance inflation factor for the final predictor variables. When developing the prediction model of the time to death based on the Cox regression analysis, we followed the transparent reporting of a multivariable prediction model for individual prognosis or diagnosis (TRIPOD) 2015 guideline [45]. For each model, we calculated the Harrell's c-statistic with optimism correction using the internal bootstrap method [13], along with apparent c-statistic. The bootstrap was replicated 1000 times. In the animal experiments, statistical significances in mean values among the groups were analyzed by analysis of variance (ANOVA) and Student's t-tests. The survival rates were analyzed by log-rank test. All the statistical analyses were performed using GraphPad Prism

software version 8.0 (GraphPad Software, San Diego, CA), EZR software version 1.54, a free software for using R on graphical user interface [46], and the SAS (version 9.4; SAS Institute Inc., Cary, NC, USA). All statistical analyses were two-sided, and statistical significance was considered as $P < 0.05$.

Acknowledgement

We thank Katsuko Yamasaki for her expert technical assistance with histological analysis. We also thank Lucinda Beck for carefully proofreading the manuscript. We would like to thank all the participants in our institute for the management of patients with COVID-19.

Competing interests

S.Y. received research funding from Abbvie, Asahi Kasei, Pharma, Chugai Pharmaceutical, CSL Behring, Eisai, ImmunoForge, Mitsubishi Tanabe, Pharma, and Ono pharmaceutical, speaking fees from Abbvie, Asahi Kasei Pharma, Chugai Pharmaceutical, Eisai, Eli Lilly, GlaxoSmithKline, Mitsubishi Tanabe Pharma, Ono pharmaceutical, and Pfizer. YM received a research grant and an honorarium from Chugai Pharmaceutical Co., Ltd. The other authors have declared no conflicts of interest.

Funding, grant/award info

SY was supported by the Japan Agency for Medical Research and Development (AMED) under grant number 21ek0410083h0002. T. Suzuki was supported by AMED under grant number JP22fk0108637 and JP22wm0125008.

Author Contribution

TH, T. Suzuki, HH, and SY conceived and designed the experiments. SO, YK, TH, DK, HI, SM, M. Kataoka, MT, TK, and AA performed the experiments. SO, YK, TH, DK, M. Kamiya, HI, SM, M. Kataoka, MT, TK, AA, HS, AH, TY, and T. Suzuki analyzed data. KW, YO, and YM collected the patient information. TH, SO, M. Kamiya, T. Satoh, KW, TY, YM, HH, T. Suzuki, and SY wrote the paper.

Data sharing statement

The data that support the findings of this study are available from the corresponding author upon request. RNA-Seq data is available in ArrayExpress (in the process of deposition).

Reference

1. Kwok S, Adam S, Ho JH, Iqbal Z, Turkington P, Razvi S, et al. Obesity: A critical risk factor in the COVID-19 pandemic. *Clin Obes.* 2020 Dec;10(6):e12403.
2. Huang C, Wang Y, Li X, Ren L, Zhao J, Hu Y, et al. Clinical features of patients infected with 2019 novel coronavirus in Wuhan, China. *Lancet (London, England).* 2020 Feb 15;395(10223):497–506.
3. Lucas C, Wong P, Klein J, Castro TBR, Silva J, Sundaram M, et al. Longitudinal analyses reveal immunological misfiring in severe COVID-19. *Nature.* 2020 Aug 20;584(7821):463–9.
4. Oba S, Hosoya T, Amamiya M, Mitsumura T, Kawata D, Sasaki H, et al. Arterial and Venous Thrombosis Complicated in COVID-19: A Retrospective Single Center Analysis in Japan. *Front Cardiovasc Med.* 2021 Nov 19;8:767074.
5. Nazare JA, Smith JD, Borel AL, Haffner SM, Balkau B, Ross R, et al. Ethnic influences on the relations between abdominal subcutaneous and visceral adiposity, liver fat, and cardiometabolic risk profile: The international study of prediction of intra-abdominal adiposity and its relationship relationship with cardiometabolic risk/intra-abdominal adiposity. *Am J Clin Nutr.* 2012;96(4):714–26.
6. Peters MC, McGrath KW, Hawkins GA, Hastie AT, Levy BD, Israel E, et al. Plasma interleukin-6 concentrations, metabolic dysfunction, and asthma severity: a cross-sectional analysis of two cohorts. *Lancet Respir Med.* 2016 Jul 1;4(7):574–84.
7. Yoshizumi T, Nakamura T, Yamane M, Waliul Islam AHM, Menju M, Yamasaki K, et al. Abdominal Fat: Standardized Technique for Measurement CT. *Radiology*. 1999 Apr;211(1):283-6.
8. Appelman B, Oppelaar JJ, Broeders L, Wiersinga WJ, Peters-Sengers H, Vogt L, et al. Mortality and readmission rates among hospitalized COVID-19 patients with varying stages of chronic kidney disease: a multicenter retrospective cohort. *Sci Reports 2022 121.* 2022 Feb 10;12(1):1–8.
9. Mubarik S, Liu X, Eshak ES, Liu K, Liu Q, Wang F, et al. The Association of Hypertension With the Severity of and Mortality From the COVID-19 in the Early Stage of the Epidemic in Wuhan, China: A Multicenter Retrospective Cohort Study. *Front Med.* 2021 May 12;8:631.
10. Peckham H, de Gruijter NM, Raine C, Radziszewska A, Ciurtin C, Wedderburn LR, et al. Male sex identified by global COVID-19 meta-analysis as a risk factor for death

and ITU admission. *Nat Commun.* 2020 Dec 9;11(1):1–10.

11. Gu T, Chu Q, Yu Z, Fa B, Li A, Xu L, et al. History of coronary heart disease increased the mortality rate of patients with COVID-19: a nested case–control study. *BMJ Open.* 2020 Sep 1;10(9):e038976.

12. Holman N, Knighton P, Kar P, O'Keefe J, Curley M, Weaver A, et al. Risk factors for COVID-19-related mortality in people with type 1 and type 2 diabetes in England: a population-based cohort study. *Lancet Diabetes Endocrinol.* 2020 Oct 1;8(10):823–33.

13. Harrell FE Jr, Lee KL, Mark DB. Multivariable prognostic models: issues in developing models, evaluating assumptions and adequacy, and measuring and reducing errors. Stat Med. 1996 Feb 28;15(4):361-87.

14. Russo L, Lumeng CN. Properties and functions of adipose tissue macrophages in obesity. *Immunology.* 2018 Dec 1;155(4):407–17.

15. Suriano F, Vieira-Silva S, Falony G, Roumain M, Paquot A, Pelicaen R, et al. Novel insights into the genetically obese (ob/ob) and diabetic (db/db) mice: two sides of the same coin. *Microbiome.* 2021;9(1):1–20.

16. Giesbertz P, Padberg I, Rein D, Ecker J, Höfle AS, Spanier B, et al. Metabolite profiling in plasma and tissues of ob/ob and db/db mice identifies novel markers of obesity and type 2 diabetes. *Diabetologia.* 2015 Sep 7;58(9):2133–43.

17. Iwata-Yoshikawa N, Shiwa N, Sekizuka T, Sano K, Ainai A, Hemmi T, et al. A lethal mouse model for evaluating vaccine-associated enhanced respiratory disease during SARS-CoV-2 infection. *Sci Adv.* 2022 Jan 1;8(1):3827.

18. Sefik E, Qu R, Junqueira C, Kaffe E, Mirza H, Zhao J, et al. Inflammasome activation in infected macrophages drives COVID-19 pathology. *Nature.* 2022 Jun;606(7914):585-593.

19. Junqueira C, Crespo Â, Ranjbar S, de Lacerda LB, Lewandrowski M, Ingber J, et al. FcγR-mediated SARS-CoV-2 infection of monocytes activates inflammation. *Nature.* 2022 Jun;606(7914):576-584.

20. Zhang YN, Zhang ZR, Zhang HQ, Li XD, Li JQ, Zhang QY, et al. Increased morbidity of obese mice infected with mouse-adapted SARS-CoV-2. *Cell Discov.* 2021;7(1): 74.

21. Okazaki M, Yamada Y, Nishimoto N, Yoshizaki K, Mihara M. Characterization of anti-mouse interleukin-6 receptor antibody. *Immunol Lett.* 2002 Dec 3;84(3):231–40.

22. Favre G, Legueult K, Pradier C, Raffaelli C, Ichai C, Iannelli A, et al. Visceral fat is associated to the severity of COVID-19. *Metabolism.* 2021 Feb 1;115:154440.

23. Scheffler M, Genton L, Graf CE, Remuinan J, Gold G, Zekry D, et al. Prognostic Role of Subcutaneous and Visceral Adiposity in Hospitalized Octogenarians with COVID-19. *J Clin Med.* 2021 Nov 24;10(23):5500.

24. Yates T, Summerfield A, Razieh C, Banerjee A, Chudasama Y, Davies MJ, et al. A population-based cohort study of obesity, ethnicity and COVID-19 mortality in 12.6 million adults in England. *Nat Commun.* 2022 Dec 1;13(1): 624.

25. Gao M, Piernas C, Astbury NM, Hippisley-Cox J, O'Rahilly S, Aveyard P, et al. Associations between body-mass index and COVID-19 severity in 6·9 million people in England: a prospective, community-based, cohort study. *lancet Diabetes Endocrinol.* 2021 Jun 1;9(6):350–9.

26. Kadowaki T, Sekikawa A, Murata K, Maegawa H, Takamiya T, Okamura T, et al. Japanese men have larger areas of visceral adipose tissue than Caucasian men in the same levels of waist circumference in a population-based study. *Int J Obes 2006 307.* 2006 Jan 31;30(7):1163–5.

27. Ge E, Li Y, Wu S, Candido E, Wei X. Association of pre-existing comorbidities with mortality and disease severity among 167,500 individuals with COVID-19 in Canada: A population-based cohort study. *PLoS One.* 2021 Oct 5;16(10):e0258154.

28. Grant RA, Morales-Nebreda L, Markov NS, Swaminathan S, Querrey M, Guzman ER, et al. Circuits between infected macrophages and T cells in SARS-CoV-2 pneumonia. *Nature.* 2021 Jan 11;590(7847):635–41.

29. Martínez-Colón GJ, Ratnasiri K, Chen H, Jiang S, Zanley E, Rustagi A, et al. SARS-CoV-2 infection drives an inflammatory response in human adipose tissue through infection of adipocytes and macrophages. *Sci Transl Med.* 2022 Sep 22:eabm9151.

30. Mitsui Y, Suzuki T, Kuniyoshi K, Inamo J, Yamaguchi K, Komuro M, et al. CiDRE+ M2c macrophages hijacked by SARS-CoV-2 cause COVID-19 severity. *bioRxiv.* 2022 Oct 3;2022.09.30.510331.

31. Zickler M, Stanelle-Bertram S, Ehret S, Heinrich F, Lange P, Schaumburg B, et al. Replication of SARS-CoV-2 in adipose tissue determines organ and systemic lipid metabolism in hamsters and humans. *Cell Metab.* 2022 Jan 4;34(1):1–2.

32. Reiterer M, Rajan M, Gómez-Banoy N, Lau JD, Gomez-Escobar LG, Ma L, et al. Hyperglycemia in acute COVID-19 is characterized by insulin resistance and

adipose tissue infectivity by SARS-CoV-2. *Cell Metab.* 2021 Nov 2;33(11):2174-2188.e5.

33. Salina AC, dos-Santos D, Rodrigues TS, Fortes-Rocha M, Freitas-Filho EG, Alzamora-Terrel DL, et al. Efferocytosis of SARS-CoV-2-infected dying cells impairs macrophage anti-inflammatory functions and clearance of apoptotic cells. *Elife.* 2022 Jun 6;11: 74443.

34. Tajbakhsh A, Seyed |, Gheibihayat M, Karami N, Amir Savardashtaki |, Butler AE, et al. The regulation of efferocytosis signaling pathways and adipose tissue homeostasis in physiological conditions and obesity: Current understanding and treatment options. *Obes Rev.* 2022 Jun 29;e13487.

35. Li S, Sun Y, Liang CP, Thorp EB, Han S, Jehle AW, et al. Defective Phagocytosis of Apoptotic Cells by Macrophages in Atherosclerotic Lesions of ob/ob Mice and Reversal by a Fish Oil Diet. *Circ Res.* 2009 Nov 20;105(11):1072–82.

36. Davis RC, Castellani LW, Hosseini M, Ben-Zeev O, Mao HZ, Weinstein MM, et al. Early Hepatic Insulin Resistance Precedes the Onset of Diabetes in Obese C57BLKS-db/db Mice. *Diabetes.* 2010 Jul 1;59(7):1616–25.

37. Thaiss CA, Levy M, Grosheva I, Zheng D, Soffer E, Blacher E, et al. Hyperglycemia drives intestinal barrier dysfunction and risk for enteric infection. *Science.* 2018 Mar 23;359(6382):1376–83.

38. Ikejima S, Sasaki S, Sashinami H, Mori F, Ogawa Y, Nakamura T, et al. Impairment of Host Resistance to Listeria monocytogenes Infection in Liver of db/db and ob/ob Mice. *Diabetes.* 2005 Jan 1;54(1):182–9.

39. Honce R, Schultz-Cherry S. Impact of obesity on influenza A virus pathogenesis, immune response, and evolution. *Front Immunol.* 2019;10(MAY):1071.

40. Faggioni R, Fantuzzi G, Gabay C, Moser A, Dinarello CA, Feingold KR, et al. Leptin deficiency enhances sensitivity to endotoxin-induced lethality. *Am J Physiol.* 1999 Jan;276(1):R136-42.

41. Wedell-Neergaard AS, Eriksen L, Grønbæk M, Pedersen BK, Krogh-Madsen R, Tolstrup J. Low fitness is associated with abdominal adiposity and low-grade inflammation independent of BMI. *PLoS One.* 2018 Jan 17;13(1):e0190645.

42. Shioya-Yamada M, Shimada K, Nishitani-Yokoyama M, Sai E, Takeno K, Tamura Y, et al. Association Between Visceral Fat Accumulation and Exercise Tolerance in Non-Obese Subjects Without Diabetes. *J Clin Med Res.* 2018;10(8):630-635.

43. Imai M, Iwatsuki-Horimoto K, Hatta M, Loeber S, Halfmann PJ, Nakajima N, et al. Syrian hamsters as a small animal model for SARS-CoV-2 infection and countermeasure development. *Proc Natl Acad Sci U S A.* 2020 Jul 14;117(28):16587–95.

44. Matute-Bello G, Frevert CW, Martin TR. Animal models of acute lung injury. *Am J Physiol - Lung Cell Mol Physiol.* 2008 Sep;295(3):379–99.

45. Moons KGM, Altman DG, Reitsma JB, Ioannidis JPA, Macaskill P, Steyerberg EW, et al. Transparent Reporting of a multivariable prediction model for Individual Prognosis Or Diagnosis (TRIPOD): Explanation and Elaboration. *Ann Intern Med.* 2015 Jan 6;162(1):W1-73.

46. Kanda Y. Investigation of the freely available easy-to-use software 'EZR' for medical statistics. *Bone Marrow Transplant 2013 483.* 2012 Dec 3;48(3):452–8.

＜Figure Legend＞

Figure1: VAT area but not the other obesity markers was associated with COVID-19 mortality and inflammatory biomarkers.

(**A**) Representative CT images analyzed by Fat Scan. The left and right panels represented visceral fat dominant obesity (apple-shaped) and subcutaneous-dominant obesity (pear-shaped), respectively. The visceral fat is indicated in red, and the subcutaneous fat is indicated in pink.

(**B-D**) The association of the peak severity and obesity-associated markers, VAT (B), BMI (C), and SAT (D). Data are mean ± SD. One-way ANOVA followed by Tukey's post hoc test was performed to compare three groups.

(**E-G**) Kaplan-Meier plot of survival rate in COVID-19 patients during hospitalization until 120 days after admission. Graph shows survival curves when patients are divided into two groups based on the VAT (E), BMI (F) and SAT (G). The cut cut-off values were designated by drawing the Receiver Operating Characteristic (ROC) curve to maximize sensitivity and specificity.

(**H-I**) Heatmap showing the correlation between obesity-associated markers and biomarkers in the patients less than 70 years old (H) and 70 years old or above (I). The correlations were evaluated by Spearman's method.

p: *: < 0,05; p: **: < 0,01; *** < 0,001. VAT: Visceral adipose tissue, BMI: Body Mass Index, SAT: Subcutaneous adipose tissue.

Figure 2: ob/ob mice were more vulnerable to SARS-CoV-2 infection with high infectivity.

(**A-B**) Survival curve (A) and body weight (B) of ob/ob, db/db, and B6 mice (n = 11-12) after mouse-adapted SARS-CoV-2 inoculation. Data are pooled from two independent experiments showing similar results. Log-rank (Mantel-Cox) test was used to assess the survival curve. Data are mean ± SD.

(**C-E**) Immunohistochemical staining using anti–SARS-CoV-2 N-specific antibody in the lungs of three strains at three days post infection (dpi) in Alveola area (D) and Bronchial area (E). IHC scores were determined based on the percentage of viral antigen-positive cells, using the following scoring system: 0, no positive cells; 1, positive cells (≤5%); 2, positive cells (>5%, ≤20%); 3, positive cells (>20%, ≤50%); 4, positive cells (>50%).

(**F-H**) The abundance of SARS-CoV-2 genomic RNA detected in the tissue samples derived from lung (F), peripheral blood (G), and liver (H) at three dpi.

(**I-K**) Semi-quantification of SARS-CoV-2 carrying macrophages by immunohistochemical (IHC) staining in the lungs of three strains at three dpi. (I) Representative image of triple IHC staining of F4/80 (brown), EpCAM (pink), and SARS-CoV-2 (blue) in the lungs. The arrow indicated SARS-CoV-2 antigens engulfed in macrophages. The arrowhead indicated SARS-CoV-2 antigens positive lung epithelial cells. (J) Representative images of SARS-CoV-2 and F4/80 double positive cells in the lungs of three strains. (K) The proportions of SARS-CoV-2 and F4/80 double positive cells in F4/80 single positive cells. One-way ANOVA followed by Tukey's post hoc test was performed to compare three groups. Data are mean ± SD. **P < 0.01, ***P < 0.001.

(**L**) Electron microscopy images of viral particles in infected ob/ob mice. A higher-magnification images of the boxed area in the bottom. Nucleocapsid-visible viral particles and high-density viral particles were indicated with black arrowhead and white arrowhead, respectively. Scale bars, 1.0 μm (top); 0.2 μm (bottom)

Figure 3: Lethal level of excessive immune responses in the lung of ob/ob mice

(**A-B**) Quantitative analysis of representative immune-related, including IL-6 and interferon signature genes relative to B6 (A), and intracellular virus sensing molecules (B). Data are presented as the mean ± SD, *P < 0.05, **P < 0.01, ***P < 0.001. Data were analyzed by one-way ANOVA followed by Tukey's post hoc test.

(**C**) Heatmap of the concentrations of immune-related cytokines and chemokines in the lung homogenates at three days post infection (dpi) (n=3 mice for each group), analyzed by Mouse Luminex Discovery Assay. The red color indicates higher concentrations of the biomarkers (pg/ml for IL-6, IL-10, TNF-α, IL-1-α, and IFN-γ, ng/ml for MCP-1, IL-33, and IP-10.)

(**D-H**) RNA sequencing analysis of lung samples from ob/ob, db/db, and B6 mice at three dpi. (D) Principal component analysis of RNA sequencing data from nine murine lung samples in the three groups at three dpi. The X and Y axes represent a data set of the corresponding principal components obtained after the dimension reduction of the sample expressions. The red, blue, and black dots and ellipses represented the sample distributions of ob/ob, db/db, and B6 mice, respectively. (E) Venn Diagram showing differentially expressed genes (DEGs) in ob/ob vs. db/db mice (green) or B6 mice (magenta), respectively. (F) The enrichment analysis of the shared 184 DEGs in Fig. 3E. The X-axis showed -log10(Q value). The dot line corresponded to a Q value = 0.05. The red bars indicated significantly enriched pathways. (G) The representative results of gene set enrichment analysis comparing ob/ob mice vs. B6 mice and db/db mice using the Gene ontology (GO) database related to biological process (GO_P). The X-axis always indicates the rank of the change value (ob/ob vs. the others). The green fold line indicates the change curve of the gene enrichment score (ES), and the Y-axis is the ES value. The numbers aside the wave top were the rank of bottom genes in the leading edges. Normalized enrichment scores of "cellular response to interferon-beta", "cellular response to interferon-gamma", "inflammatory response", "monocyte chemotaxis" were 3.8, 2.8, 2.7 and 2.7, respectively. (H) The heatmap of representative gene transcriptions in the top four pathways in Fig. 3F. The TPM Z-scores were standardized by row direction. The red and blue colors indicated higher and lower scores.

(**I**) The survival curve of vehicle (n=22), control IgG (n=18), or MR16-1 (n=17) administrated mice are shown. Data are pooled from three independent experiments showing similar results. The agents were administered intraperitoneally one hour before infection and at three dpi. Log-rank (Mantel-Cox) test was used to assess the survival curve.

Figure 4: Lean ob/ob mice survived after SARS-CoV-2 infection by inducing an appropriate immune reaction

(**A**) Survival curve after mouse-adapted SARS-CoV-2 inoculation. The groups consisted of vehicle (n=11), 2ug/day of leptin pretreatment (n=8), 10ug/day of leptin pretreatment (n=8), 2ug/day of leptin after infection (n=4) and 10ug/day of leptin after infection (n=3). Data are pooled from three independent experiments showing similar results. Log-rank (Mantel-Cox) test was used to assess the survival curve.

(**B-F**) Comparison of mice received vehicle (n=5) or 2ug/day of leptin pretreatment (N=5) at three days post infection (dpi). Immunohistochemical staining of the lung using anti–SARS-CoV-2 N-specific antibody (B). Quantitative analysis of SARS-CoV-2 genomic RNA (C), IL-6 (E) and interferon signature genes (F). The proportions of SARS-CoV-2 and F4/80 double positive cells in F4/80 single positive cells (D). A student t-test was used to compare two groups. Data are presented as the mean ± SD. *P < 0.05, **P < 0.01, ***P < 0.001.

(**G-J**) RNA sequencing analysis comparing the immune responses of lean ob/ob mice to obese ob/ob mice at three dpi. (G) Principal component analysis of RNA sequencing data from nine murine lung samples from vehicle treated (obese ob/ob, n=3), 2ug/day of leptin pretreatment (lean ob/ob, n=3), and 2ug/day of leptin after infection (obese ob/ob with leptin, n=3). The red, blue, and black dots and ellipses represented the sample distributions of individual mouse in three groups. (H) Venn Diagram showing differentially expressed genes (DEGs) in Lean ob/ob vs. obese ob/ob (magenta), or obese ob/ob with leptin (green), respectively. (I) The pathway enrichment analysis of the shared 689 DEGs shown in Fig. 4H. The X-axis showed -log10(Q value). The dot line corresponded to a Q value = 0.05. The red bars indicated significantly enriched pathways. (J) The representative results of gene set enrichment analysis comparing obese ob/ob mice vs. lean ob/ob using the Gene ontology (GO) database related to biological process (GO_P). The X-axis always indicates the rank of the change value (ob/ob mice vs. lean ob/ob). Normalized enrichment scores of "cellular response to interferon-beta", "cellular response to interferon-gamma", "inflammatory response“, and "monocyte chemotaxis“ were -3.0, -2.1, -2.1 and -1.9, respectively.

Extended Data Table 1: Comparison of baseline characteristics including obesity associated markers and comorbidities in deceased and survive patients with COVID-19

Extended Data Table 2: Univariable and multivariable logistic regression analysis adjusted for the variables.

Extended Data Table 3: Harrell's c-statistic for Cox regression model for predicting time to death

Extended Data Figure 1: The associations between VAT and inflammatory markers at the disease peak

(**A-C**) Correlation between VAT area and biomarkers at the disease peak in the patients less than 70 years old (red dots) and 70 years old or above (black dots). The correlations were evaluated by Spearman's method.

Extended Data Figure 2: Different patterns of adipose tissue distribution in aged ob/ob and db/db mice

(**A**) Body weight of ob/ob, db/db, and B6 mice at 19 weeks. One-way ANOVA with posthoc Tukey Test was used to compare three groups. Data were mean ± SD.

(**B**) Representative images of the adipose tissue in ob/ob mice and db/db mice.

(**C**) Comparison of visceral and subcutaneous adipose tissues. VAT was perirenal fat, and SAT was the sum of inguinal and hip adipose tissues. A student t-test was used to compare two groups. Data were mean ± SD. p: *: < 0,05; p: **: < 0,01; *** < 0,001. VAT: Visceral adipose tissue, BMI: Body Mass Index, SAT: Subcutaneous adipose tissue.

Extended Data Figure 3: ob/ob mice showed broad inflammation in the lung, while tissue damage was comparable

(**A-C**) Pulmonary pathological scores for mice (n=5 or 6 per group) at three days post infection (dpi). The distribution scores (A) and the acute lung injury (ALI) score (B) were determined from the average of five lobes in individual mice.

One-way ANOVA followed by Tukey's post hoc test) was performed to compare three groups. Data are mean ± SD. **P < 0.01, ***P < 0.001.

Extended Data Figure 4: Indifferent virus susceptibility of the lung cells among three strains

(**A-C**) Immunohistochemical staining of the lung using anti–SARS-CoV-2 N-specific antibody at one day post infection (dpi). IHC scores were determined based on the percentage of viral antigen-positive cells, using the following scoring system: 0, no positive cells; 1, positive cells (≤5%); 2, positive cells (>5%, ≤20%); 3, positive cells (>20%, ≤50%); 4, positive cells (>50%). One-way ANOVA followed by Tukey's post hoc test) was performed to compare three groups. Data are mean ± SD.

(**D**) Viral infectivity in the lung homogenates analyzed on one dpi and three dpi (n=3 per group). Data are mean TCID50 ± SD.

(**E**) Non-hematopoietic lung cells from non-infected ob/ob and db/db mice (n=4) were infected with SARS-CoV-2 (QHmusX) at different multiplicity of infection (MOI). Cell lysates were prepared for RT-PCR of SARS-CoV-2 genomic RNA.

Extended Data Figure 5: RNA-Seq analysis of ob/ob and db/db mice under non-infected and infected conditions

(**A**) Principal component analysis of RNA sequencing data from 18 samples of ob/ob mice and db/db mice under non-infected or infected conditions. The X and Y axes represent a data set of the corresponding principal components obtained after the dimension reduction of the sample expressions. The dots and ellipses represented the sample distributions of ob/ob mice and db/db mice under non-infected or infected conditions.

(**B**) Venn Diagram showing differentially expressed genes (DEGs) in ob/ob vs. db/db mice under non-infected (green) or infected (magenta) conditions, respectively. Genes expressing significantly different amounts between the paired groups were determined using the PossionDis method and DESeq2. FDR ≤ 0.001 in PossionDis and Q value (adjusted P value) ≤0.05 in DESeq2 were considered as cutoffs.

(**C**) The enrichment analysis of the shared 738 DEGs in non-infected conditions. For the pathway classification, Kyoto Encyclopedia of Genes and Genomes (KEGG) annotation was used. The X-axis showed -log10(Q value). The dotted line corresponds to a Q value = 0.05. The red bars indicated significantly enriched pathways.

(**D**) The heatmap of DEGs in the phagosome pathway in non-infected ob/ob and db/db mice. The TPM Z-scores were standardized by row direction. The red and blue colors indicated higher and lower scores.

(**E**) The heat map of the representative macrophage phenotype associated genes of ob/ob and db/db mice under non-infected and infected conditions. Genes were categorized as pan; pan-macrophage markers; M1, inflammatory macrophage makers, and M2, anti-inflammatory macrophage markers. The TPM Z-scores were standardized by row direction. The red and blue colors indicated higher and lower scores.

Extended Data Figure 6: Adipose tissue reduction by continuous leptin administration

(**A-F**) The effects of pre-treatment of leptin in ob/ob mice. (A) The body weight before infection related to Fig. 4A. Data were mean ± SD. (B) Representative images of the mice with vehicle or leptin pre-treatment. (C) The weight of adipose tissues in the leptin or vehicle treated mice. The definitions of VAT and SAT are the same in Extended Data Figure 2. (D) The representative images of IHC staining in the liver using F4/80 antibody. The arrowheads indicated the crown-like structures (CLS). (E) The number of CLSs around portal veins. A student t-test was used to compare two groups. Data were mean ± SD. p: *: < 0,05; p: **: < 0,01; *** < 0,001.

Extended Data Figure 7: Abdominal adipose accumulation exacerbated the outcome of SARS-CoV-2 infection in wild type mice

(**A-D**) Survival curve of normal fat diet (NFD) (n=12) and high fat diet (HFD) (n=13) after mouse-adapted SARS-CoV-2 inoculation (A). Log-rank (Mantel-Cox) test was used to assess the survival curve. Representative images of the mice fed by NFD or HFD (B). The sequential change of body weight during HFD feeding (C) and the comparison of body weight in NFD and HFD groups before infection(D). A student t-test was used to compare two groups. Data were mean ± SD. p: *** < 0,001.

Figures

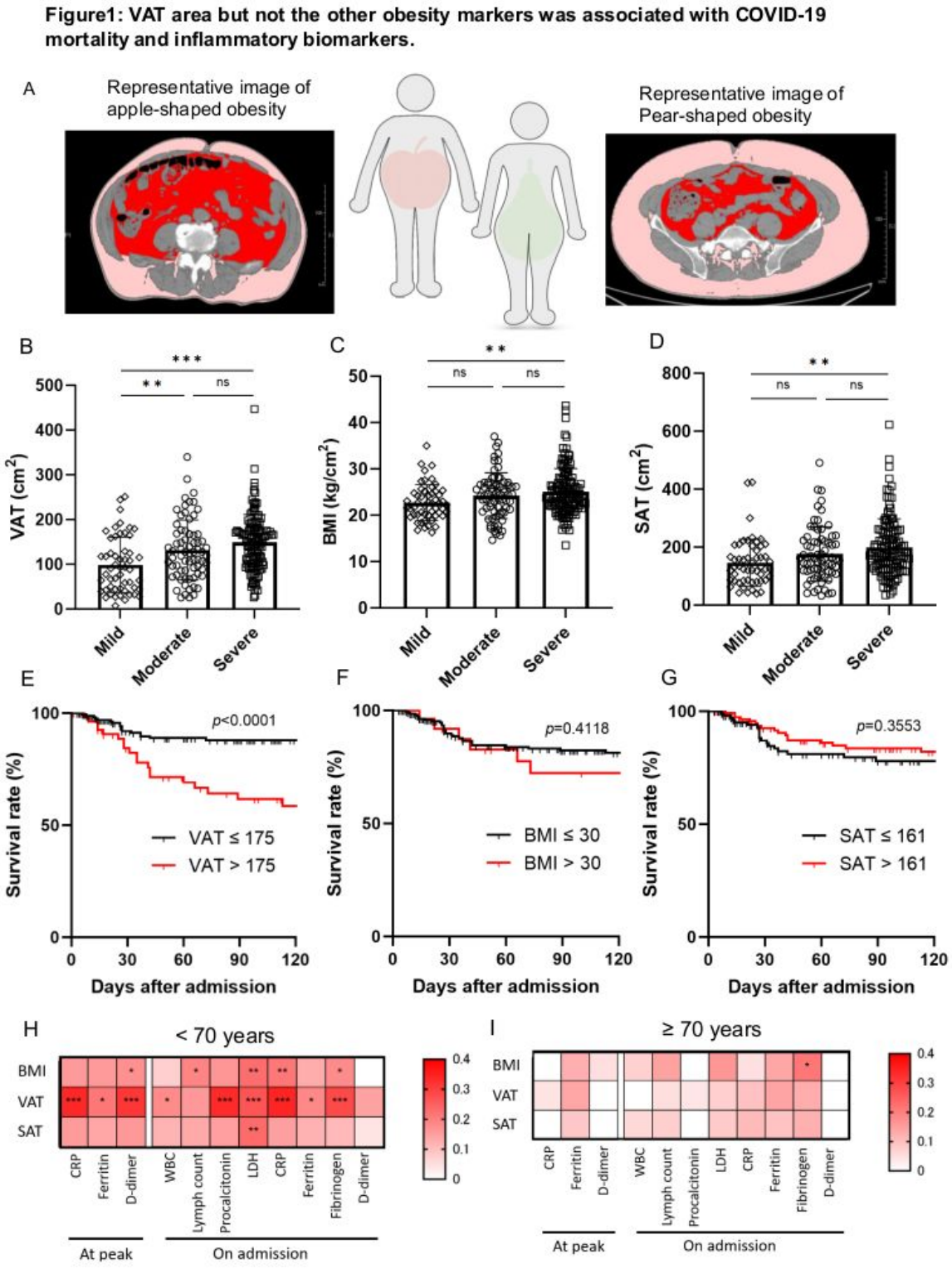

Figure 1

VAT area but not the other obesity markers was associated with COVID-19 mortality and inflammatory biomarkers. (A) Representative CT images analyzed by Fat Scan. The left and right panels represented visceral fat dominant obesity (apple-shaped) and subcutaneous-dominant obesity (pear-shaped),

respectively. The visceral fat is indicated in red, and the subcutaneous fat is indicated in pink. (B-D) The association of the peak severity and obesity-associated markers, VAT (B), BMI (C), and SAT (D). Data are mean ± SD. One-way ANOVA followed by Tukey's post hoc test was performed to compare three groups. (E-G) Kaplan-Meier plot of survival rate in COVID-19 patients during hospitalization until 120 days after admission. Graph shows survival curves when patients are divided into two groups based on the VAT (E), BMI (F) and SAT (G). The cut cut-off values were designated by drawing the Receiver Operating Characteristic (ROC) curve to maximize sensitivity and specificity. (H-I) Heatmap showing the correlation between obesity-associated markers and biomarkers in the patients less than 70 years old (H) and 70 years old or above (I). The correlations were evaluated by Spearman's method. p: *: < 0,05; p: **: < 0,01; *** < 0,001. VAT: Visceral adipose tissue, BMI: Body Mass Index, SAT: Subcutaneous adipose tissue.

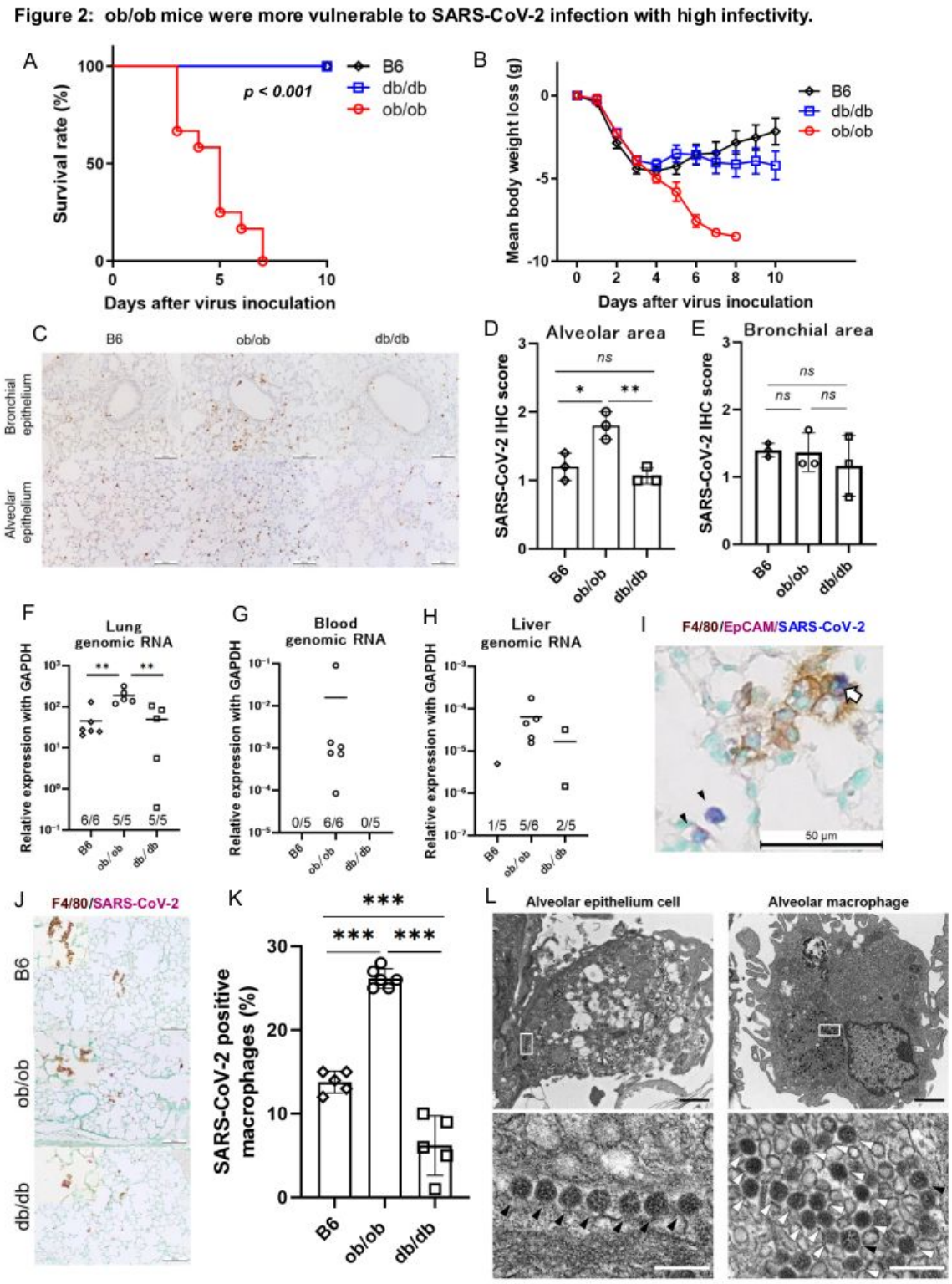

Figure 2

ob/ob mice were more vulnerable to SARS-CoV-2 infection with high infectivity. (A-B) Survival curve (A) and body weight (B) of ob/ob, db/db, and B6 mice (n = 11-12) after mouseadapted SARS-CoV-2 inoculation. Data are pooled from two independent experiments showing similar results. Log-rank (Mantel-Cox) test was used to assess the survival curve. Data are mean ± SD. (C-E) Immunohistochemical staining using anti–SARS-CoV-2 N-specific antibody in the lungs of three strains

at three days post infection (dpi) in Alveola area (D) and Bronchial area (E). IHC scores were determined based on the percentage of viral antigen-positive cells, using the following scoring system: 0, no positive cells; 1, positive cells (≤5%); 2, positive cells (>5%, ≤20%); 3, positive cells (>20%, ≤50%); 4, positive cells (>50%). (F-H) The abundance of SARS-CoV-2 genomic RNA detected in the tissue samples derived from lung (F), peripheral blood (G), and liver (H) at three dpi. (I-K) Semi-quantification of SARS-CoV-2 carrying macrophages by immunohistochemical (IHC) staining in the lungs of three strains at three dpi. (I) Representative image of triple IHC staining of F4/80 (brown), EpCAM (pink), and SARS-CoV-2 (blue) in the lungs. The arrow indicated SARS-CoV-2 antigens engulfed in macrophages. The arrowhead indicated SARS-CoV-2 antigens positive lung epithelial cells. (J) Representative images of SARS-CoV-2 and F4/80 double positive cells in the lungs of three strains. (K) The proportions of SARS-CoV-2 and F4/80 double positive cells in F4/80 single positive cells. Oneway ANOVA followed by Tukey's post hoc test was performed to compare three groups. Data are mean ± SD. **P < 0.01, ***P < 0.001. (L) Electron microscopy images of viral particles in infected ob/ob mice. A higher-magnification images of the boxed area in the bottom. Nucleocapsid-visible viral particles and high-density viral particles were indicated with black arrowhead and white arrowhead, respectively. Scale bars, 1.0 μm (top); 0.2 μm (bottom)

Figure 3: Lethal level of excessive immune responses in the lung of ob/ob mice

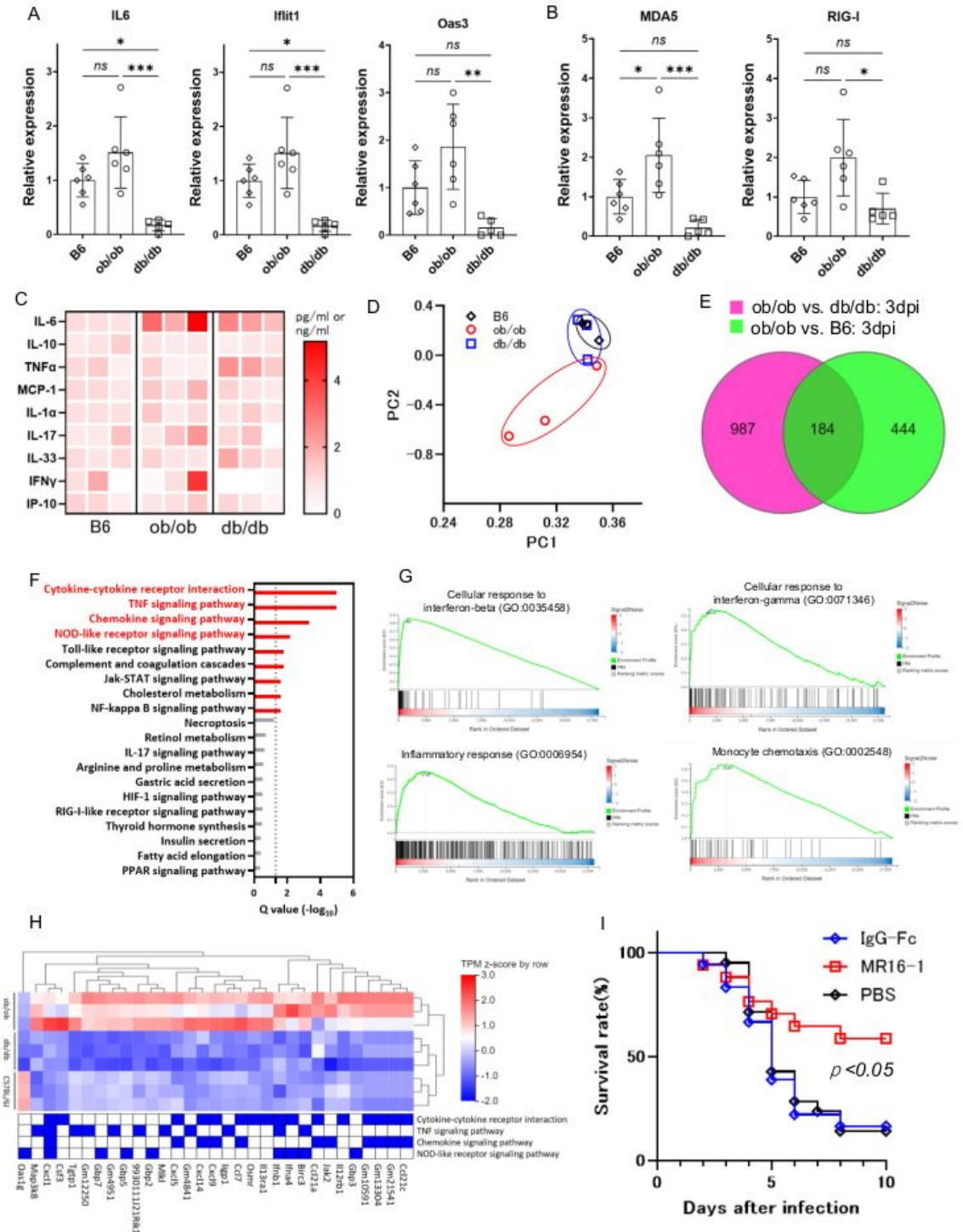

Figure 3

Lethal level of excessive immune responses in the lung of ob/ob mice (A-B) Quantitative analysis of representative immune-related, including IL-6 and interferon signature genes relative to B6 (A), and intracellular virus sensing molecules (B). Data are presented as the mean ± SD, *P < 0.05, **P < 0.01, ***P < 0.001. Data were analyzed by one-way ANOVA followed by Tukey's post hoc test. (C) Heatmap of the concentrations of immune-related cytokines and chemokines in the lung homogenates at three days post

infection (dpi) (n=3 mice for each group), analyzed by Mouse Luminex Discovery Assay. The red color indicates higher concentrations of the biomarkers (pg/ml for IL-6, IL-10, TNF-α, IL-1-α, and IFN-γ, ng/ml for MCP-1, IL-33, and IP-10.) (D-H) RNA sequencing analysis of lung samples from ob/ob, db/db, and B6 mice at three dpi. (D) Principal component analysis of RNA sequencing data from nine murine lung samples in the three groups at three dpi. The X and Y axes represent a data set of the corresponding principal components obtained after the dimension reduction of the sample expressions. The red, blue, and black dots and ellipses represented the sample distributions of ob/ob, db/db, and B6 mice, respectively. (E) Venn Diagram showing differentially expressed genes (DEGs) in ob/ob vs. db/db mice (green) or B6 mice (magenta), respectively. (F) The enrichment analysis of the shared 184 DEGs in Fig. 3E. The X-axis showed -log10(Q value). The dot line corresponded to a Q value = 0.05. The red bars indicated significantly enriched pathways. (G) The representative results of gene set enrichment analysis comparing ob/ob mice vs. B6 mice and db/db mice using the Gene ontology (GO) database related to biological process (GO_P). The X-axis always indicates the rank of the change value (ob/ob vs. the others). The green fold line indicates the change curve of the gene enrichment score (ES), and the Yaxis is the ES value. The numbers aside the wave top were the rank of bottom genes in the leading edges. Normalized enrichment scores of "cellular response to interferon-beta", "cellular response to interferon-gamma", "inflammatory response", "monocyte chemotaxis" were 3.8, 2.8, 2.7 and 2.7, respectively. (H) The heatmap of representative gene transcriptions in the top four pathways in Fig. 3F. The TPM Z-scores were standardized by row direction. The red and blue colors indicated higher and lower scores. (I) The survival curve of vehicle (n=22), control IgG (n=18), or MR16-1 (n=17) administrated mice are shown. Data are pooled from three independent experiments showing similar results. The agents were administered intraperitoneally one hour before infection and at three dpi. Log-rank (Mantel-Cox) test was used to assess the survival curve.

Figure 4: Lean ob/ob mice survived after SARS-CoV-2 infection by inducing an appropriate immune reaction

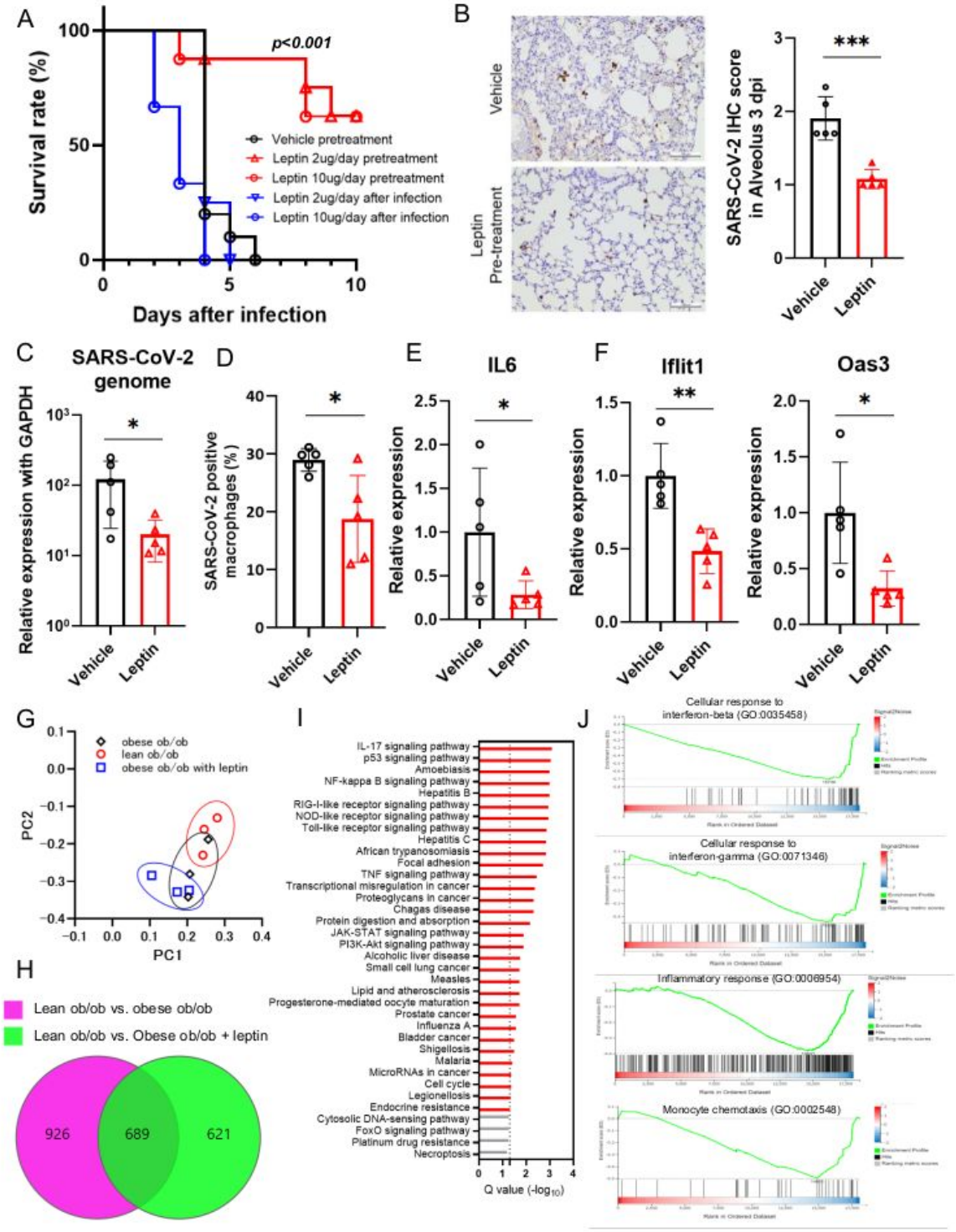

Figure 4

Lean ob/ob mice survived after SARS-CoV-2 infection by inducing an appropriate immune reaction (A) Survival curve after mouse-adapted SARS-CoV-2 inoculation. The groups consisted of vehicle (n=11), 2ug/day of leptin pretreatment (n=8), 10ug/day of leptin pretreatment (n=8), 2ug/day of leptin after infection (n=4) and 10ug/day of leptin after infection (n=3). Data are pooled from three independent experiments showing similar results. Log-rank (Mantel-Cox) test was used to assess the survival curve.

(B-F) Comparison of mice received vehicle (n=5) or 2ug/day of leptin pretreatment (N=5) at three days post infection (dpi). Immunohistochemical staining of the lung using anti–SARS-CoV-2 N-specific antibody (B). Quantitative analysis of SARS-CoV-2 genomic RNA (C), IL-6 (E) and interferon signature genes (F). The proportions of SARS-CoV-2 and F4/80 double positive cells in F4/80 single positive cells (D). A student t-test was used to compare two groups. Data are presented as the mean ± SD. *P < 0.05, **P < 0.01, ***P < 0.001. (G-J) RNA sequencing analysis comparing the immune responses of lean ob/ob mice to obese ob/ob mice at three dpi. (G) Principal component analysis of RNA sequencing data from nine murine lung samples from vehicle treated (obese ob/ob, n=3), 2ug/day of leptin pretreatment (lean ob/ob, n=3), and 2ug/day of leptin after infection (obese ob/ob with leptin, n=3). The red, blue, and black dots and ellipses represented the sample distributions of individual mouse in three groups. (H) Venn Diagram showing differentially expressed genes (DEGs) in Lean ob/ob vs. obese ob/ob (magenta), or obese ob/ob with leptin (green), respectively. (I) The pathway enrichment analysis of the shared 689 DEGs shown in Fig. 4H. The X-axis showed -log10(Q value). The dot line corresponded to a Q value = 0.05. The red bars indicated significantly enriched pathways. (J) The representative results of gene set enrichment analysis comparing obese ob/ob mice vs. lean ob/ob using the Gene ontology (GO) database related to biological process (GO_P). The X-axis always indicates the rank of the change value (ob/ob mice vs. lean ob/ob). Normalized enrichment scores of "cellular response to interferon-beta", "cellular response to interferon-gamma", "inflammatory response“, and "monocyte chemotaxis“ were -3.0, -2.1, -2.1 and - 1.9, respectively

Supplementary Files

This is a list of supplementary files associated with this preprint. Click to download.

- SuppFig1.jpg
- SuppFigure2.jpg
- SuppFigure3.jpg
- SuppFigure4.jpg
- SuppFigure5.jpg
- SuppFIgure6.jpg
- SuppFIgure7.jpg
- SuppTables1and2.jpg
- SuppTable3.jpg